

Ghost imaging with paired x-ray photonsA. Schori,^{1,2} D. Borodin,^{1,2} K. Tamasaku,² and S. Shwartz^{1,2,*}¹*Physics Department and Institute of Nanotechnology, Bar Ilan University, Ramat Gan, 52900 Israel*²*RIKEN SPring-8 Center, 1-1-1 Koto, Sayo-cho, Sayo-gun, Hyogo 679-5148, Japan*

(Received 19 December 2017; published 4 June 2018)

We report the experimental observation of ghost imaging with paired x-ray photons, which are generated by parametric downconversion. We use the one-to-one relation between the photon energies and the emission angles and the anticorrelation between the k -vectors of the signal and the idler photons to reconstruct the images of slits with nominally zero background levels. Further extension of our procedure can be used for the observation of various quantum phenomena at x-ray wavelengths.

DOI: [10.1103/PhysRevA.97.063804](https://doi.org/10.1103/PhysRevA.97.063804)**I. INTRODUCTION**

Parametric downconversion (PDC) is one of the major sources for the generation of nonclassical states of light [1–4]. This type of radiation can be used to study fundamental quantum phenomena and lead to many fascinating applications [1–4]. Indeed, numerous quantum optics effects have been demonstrated by using visible and infrared radiation. In contrast, while several papers described the observation of x-ray PDC [5–9] and a scheme for its application as a source for polarization-entangled states has been proposed [10], but to our knowledge the use of the x-ray photon pairs that are generated by PDC has never been reported. Implementation of concepts of quantum optics such as interaction-free measurements [11] and sub-shot-noise measurements [12] could be very advantageous for measurements at x-ray wavelengths since they can be used to reduce the dose of x rays that interact with samples while enhancing the resolution and contrast of the measurements and even for radiation-damage-free measurements [11]. The existence of commercially available x-ray detectors with the capability to resolve the number of photons and with near-unity quantum efficiency is appealing for testing concepts of quantum physics since these properties can be used to remedy many of the fundamental challenges of conventional quantum optics with optical radiation.

One of the well-studied applications of PDC in the optical regime is as a generator of correlated (or anticorrelated) photon pairs for quantum ghost imaging (GI) experiments [13–17]. It should be noted that while GI has been observed also with classical sources [18–25], the classical experiments do not show the important properties of quantum states of light such as the violation of the Heisenberg uncertainty principle with regards to position and momentum [26] and sub-shot-noise imaging [12]. The latter can lead to damage-free imaging, which is one of the greatest challenges of x-ray imaging.

In a typical scheme of GI, one of the photons is scattered from the object and is collected by a single-pixel detector, which does not provide sufficient information to reconstruct

the image. The second photon, which does not interact with the object, is collected by a multipixel detector, which provides the spatial resolution. However, this detector does not provide any direct information on the object, and hence the reconstruction of the image is done by correlating the data from the two detectors. GI with photon pairs can be observed by using either the spatial correlations between the photons or the anticorrelations between their k -vectors.

Similar to the optical regime, the photon pairs that are generated by x-ray PDC are correlated in space and their k -vectors are anticorrelated and therefore can be used for the demonstration of GI. PDC in the x-ray regime is supported by the plasmlike nonlinearity, which is a second-order nonlinear process that is nonzero even in centrosymmetric materials [10]. This nonlinearity is orders of magnitude weaker than typical nonlinearities in the optical regime. However, the number of modes of the quantum fluctuations, which are the driving mechanism for PDC, scale as the cube of the frequencies of the pertinent waves, thus leading to measurable coincidence count rates. Since those wavelengths are on the order of 1 Å, which is on the order of the distance between atomic planes in crystals, phase matching is achieved by using a reciprocal lattice vector as described in Fig. 1(a). These very small wavelengths imply also that the diffraction limit resolution of x rays is on the order of the atomic scale.

In this paper, we describe measurements of GI, which are based on x-ray PDC. We use the anticorrelations between the k -vectors of x-ray photon pairs to reconstruct images of 2- and 4-mm slits with nominally zero background levels. This application for x-ray photon pairs that are generated by PDC can advance the possibilities of using this type of source for the observations of quantum effects with x rays. This is important since to date there are only a few demonstrations of quantum optics at x-ray wavelengths, which were obtained by using Mössbauer nuclei [27–30], but to our knowledge no demonstration of x-ray quantum optics with PDC has been reported. The use of PDC for quantum optics is expected to open many possibilities similar to the optical regime. We note that our experiment is fundamentally different from the recent observations of classical GI at x-ray wavelengths where the source for the correlations was diffraction from speckles [21–25]. However, since the sources for the correlations in

*Sharon.shwartz@biu.ac.il

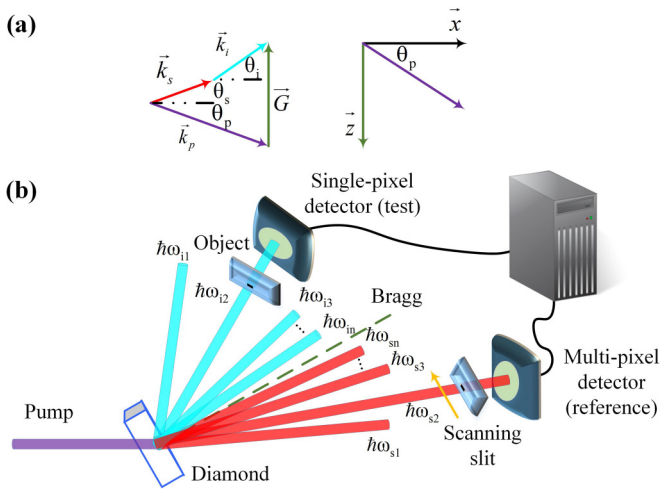


FIG. 1. (a) Phase-matching scheme. The indices p , s , and i correspond to the pump, the signal, and the idler, respectively. \vec{G} is the reciprocal lattice vector, and the angles θ_p , θ_s , and θ_i are the angles with respect to the atomic planes of the pump, the signal, and the idler, respectively. (b) Schematic of the experimental setup. The spatial resolution of the reference detector is implemented by using a scanning slit (the scanning direction is denoted by the yellow arrow). The object is mounted close to the single-pixel detector and the distance between the two detectors and the nonlinear crystal is 1050 mm. The angular spread of the downconverted signals represents the one-to-one relation between the k -vectors and the photon energies of the signal and the idler photons, denoted as $\hbar\omega_s$ and $\hbar\omega_i$, respectively. The dashed line represents the direction of Bragg diffraction.

those observations are classical they cannot be used for the demonstration of quantum physics phenomena.

In contrast to most experiments in the optical regime our experimental scheme relies on the angular spread of the k -vectors of the generated pairs, which is broader than the angular width of the object as we illustrate in Fig. 1(b). The reason for the large angular spread is the momentum conservation of the PDC process (phase matching), which uses the reciprocal lattice vector [8,9]. The noncollinear phase-matching condition, which we depict in Fig. 1(b), can be written as $\vec{k}_p + \vec{G} = \vec{k}_s + \vec{k}_i$, where \vec{k}_p , \vec{k}_s , and \vec{k}_i are the k -vectors of the pump, the signal, and the idler respectively. \vec{G} is the reciprocal lattice vector orthogonal to the atomic planes. We denote θ_p , θ_s , and θ_i as the angles with respect to the atomic planes of the pump, the signal, and the idler, respectively. The energy conservation implies that $\omega_p = \omega_s + \omega_i$, where we denote ω_p , ω_s , and ω_i as the angular frequencies of the pump, the signal, and the idler, respectively. An important consequence of the phase matching and the energy conservation is the one-to-one relation between the k -vectors and the photon energies of the signal and idler photons. We use this property for the reconstruction of the ghost images.

II. EXPERIMENT

A. Experimental system

We conducted the experiments described below at the RIKEN SR physics beamline (BL19LXU) of SPring-8 [31]

(see the Appendix for details). The schematic of the experimental system is shown in Fig. 1(b). The dimensions of the input beam are 0.5 mm (horizontal) \times 0.7 mm (vertical). To suppress the noise from Compton and Bragg scattering, we use a geometry where the angles between the emerging photon pairs, which are nearly collinear, and the input beam is close to 90° and the pump polarization is in the scattering plane [9]. We implement this geometry by working with a pump beam at 22.3 keV and by using the reciprocal lattice vector normal to the C(660) atomic planes with Laue geometry for phase matching. The Bragg angle in this geometry is 41.5° . The pump deviation from the Bragg angle at the phase-matching condition is 10 mdeg. The degenerate photon energies of the signal and idler are 11.15 keV, where the angular separation between the detectors is $\sim 2.1^\circ$.¹ One of the beams emerging from the nonlinear crystal passes through the object and is collected by a silicon drift detector (SDD), which is located behind the object and that we denote as the test detector. The second beam is collected by a 0.5 ± 0.025 -mm slit and a second SDD that we denote as the reference detector. We resolve the angular dependence of the coincidence count rates by moving the 0.5-mm slit and reference detector together across the horizontal direction with a scanning resolution of 0.5 mm (the corresponding angular resolution is $\sim 0.029^\circ$). We measured the coincidence count rate of the x-ray pairs by using coincidence electronics that records only photons that hit the two detectors within a time window of about 120 ns. We filter out false coincidences by registering only events where the sum of the energies from the two detectors is equal to the pump energy within an energy window of 1 keV.

B. Coincidence spectra

Since our GI procedure relies on the anticorrelations between the k -vectors of the signal and idler photons and on the one-to-one correspondence between the k -vectors and the photon energies of the pairs, we begin by verifying these properties. In Figs. 2 and 3 we present the coincidence spectra for the reference detector (left column) and the test detector (right column) measured with 4- and 2-mm slits, respectively. The first row shows the three-dimensional plots of the coincidence count rates as a function of the photon energy and of the position of the reference slit² measured at the reference and test detectors, respectively. In the second to the fourth rows of Fig. 2 and the second and third rows of Fig. 3 we show the spectra at a specific position of the reference slit. The blue bars are the experimental results and the solid red lines are calculated from theory and scaled to the peak of the spectra of the reference detector.³

The bright diagonal areas near the center of the spectra in panels (a1) and (a2) of Figs. 2 and 3 correspond to the x-ray pairs that are generated by the PDC process. As we expect, the

¹The errors are determined by the size of the largest slit and are 0.11° and 0.23° for the 2- and 4-mm slits, respectively.

²Which is equivalent to the angular difference for the small angular ranges.

³The description of our theoretical calculation has been described in previous papers [8,9] and is also described in detail in the Appendix.

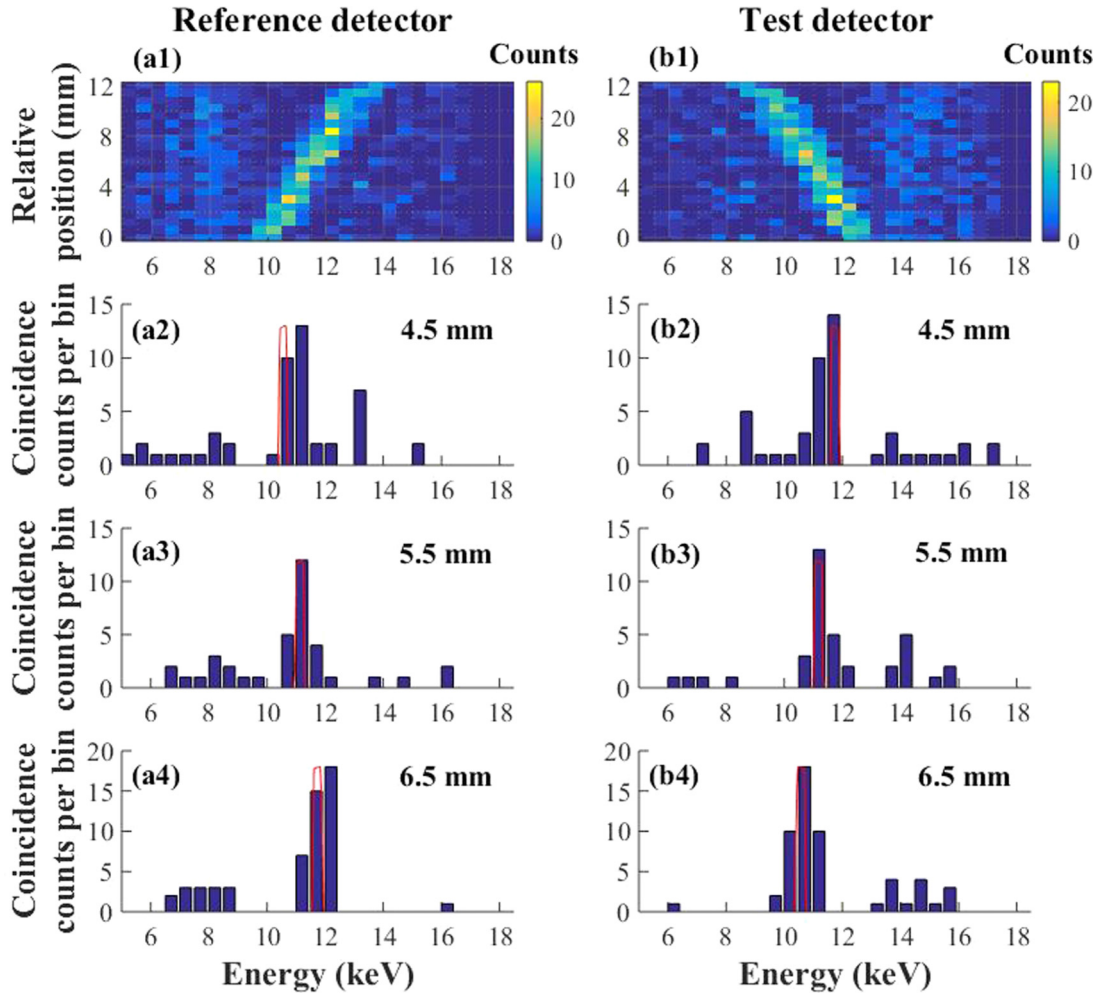


FIG. 2. Energy spectra of the coincidence counts for the 4-mm slit: reference detector (left column) and the test detector (right column). (a1,b1) Coincidence counts as a function of the photon energy and of the position of the reference slit. (a2–a4) and (b2–b4) Spectra of the coincidence counts at various positions of the reference slit. The blue bars are the experimental results and the solid red lines are calculated from theory and scaled to the peak of the spectra of the reference detector.

PDC coincidence spectra shift with the position of the reference slit due to the one-to-one relation between the photon energies and the emission angles. Of importance, our analysis of the raw data confirms that the PDC spectra are independent of the bandwidth of the energy filter. It is clear from the spectra at the various positions of the reference slit in panels (a2–a4) and (b2–b4) of Fig. 2 and in panels (a2,a3) and (b2,b3) of Fig. 3 that the measured central photon energies of the PDC process agree with the theory within the energy resolution of the detection system (we expect a spectral shift as a result of the position of the reference slit of ~ 0.5 keV/mm and measure a spectral shift of 0.4 ± 0.125 keV/mm for the 4-mm slit and 0.4 ± 0.25 keV/mm for the 2-mm slit). It is also clear that the PDC spectra are well separated from the background.

By comparing panels (a1) and (b1) of Figs. 2 and 3, we conclude that the energy range of the PDC process in Fig. 3 is smaller than in Fig. 2. This is due to the smaller acceptance angle of the 2-mm slit, which restricts the number of PDC modes. The dependence of the spectrum on the 0.5-mm slit position in Figs. 2 and 3 suggests that the energy resolution of our system is sufficient for the reconstruction of the images of the slits.

We note that since the width of the measured PDC spectrum is proportional to the width of the narrowest used slit [8] (see the Appendix for details), it is possible to resolve the widths of the slits without using any direct spatial measurement. This can be done by simply measuring the coincidence spectra and by using the one-to-one relation between the photon energies and the k -vectors of the photon pairs. The widths of the spectra that we obtain by summing up the data at the different positions of the reference slit for the 4- and 2-mm slits are 2 ± 0.25 and 1 ± 0.25 keV, respectively, and ~ 2.2 and ~ 1 keV for our numerical simulations and are in agreement within the energy bandwidth of our system (see the Appendix for details).

C. Ghost imaging

After verifying that the spectrum shifts with the position of the reference detector, we show that this property can be used to demonstrate GI. We use the coincidence measurements of the spectra in Figs. 2 and 3 to reconstruct the ghost images of the slits by counting the photon pairs with photon energies of the reference detector in a bandwidth between 11 and

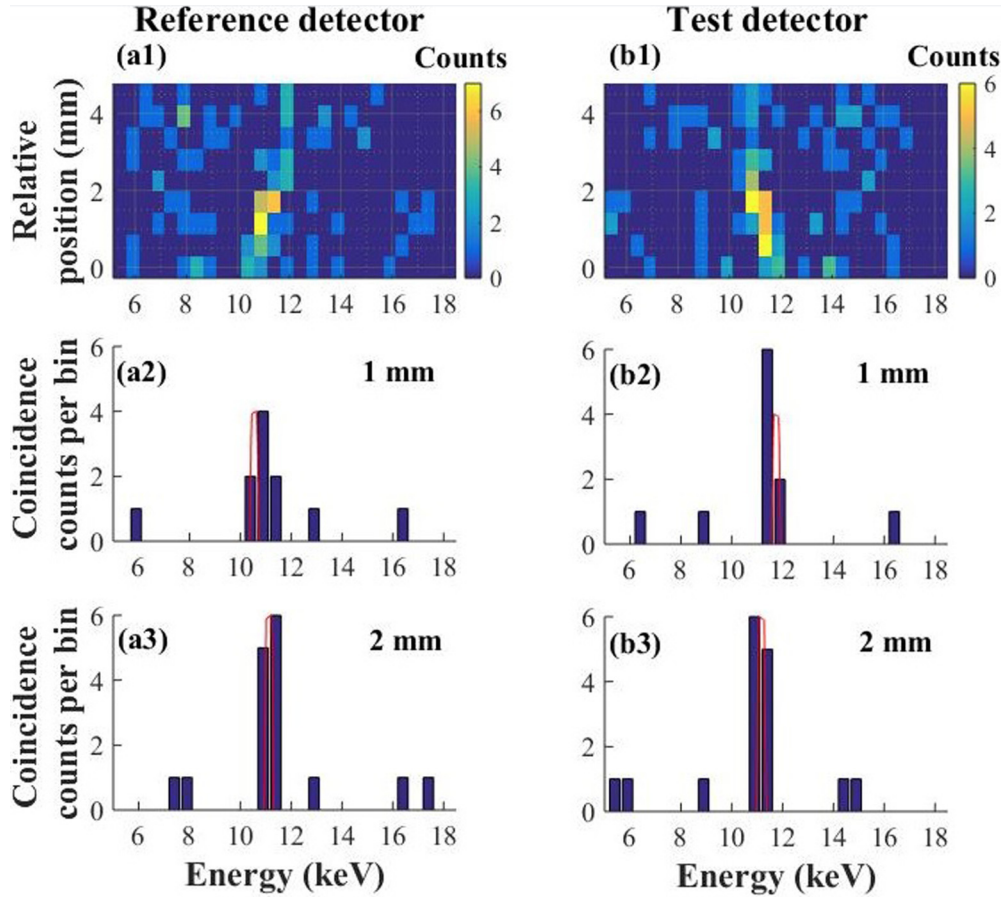


FIG. 3. Energy spectra of the coincidence counts for the 2-mm slit: reference detector (left column) and the test detector (right column). (a1,b1) Coincidence counts as a function of the photon energy and of the position of the reference slit. (a2–a3) and (b2–b3) Spectra of the coincidence count rates at various positions of the reference slit. The blue bars are the experimental results and the solid red lines are calculated from theory and scaled to the peak of the spectra of the reference detector.

11.5 keV at each of the positions of the scanning slit. We corrected the reconstructed images to account for the round shape of the detectors. GI and direct imaging of the 4-mm

slit and of the 2-mm slit are shown in panels (a) and (b), respectively, of Fig. 4. The measured slit widths at the full width at half maximum by GI and by direct imaging are in

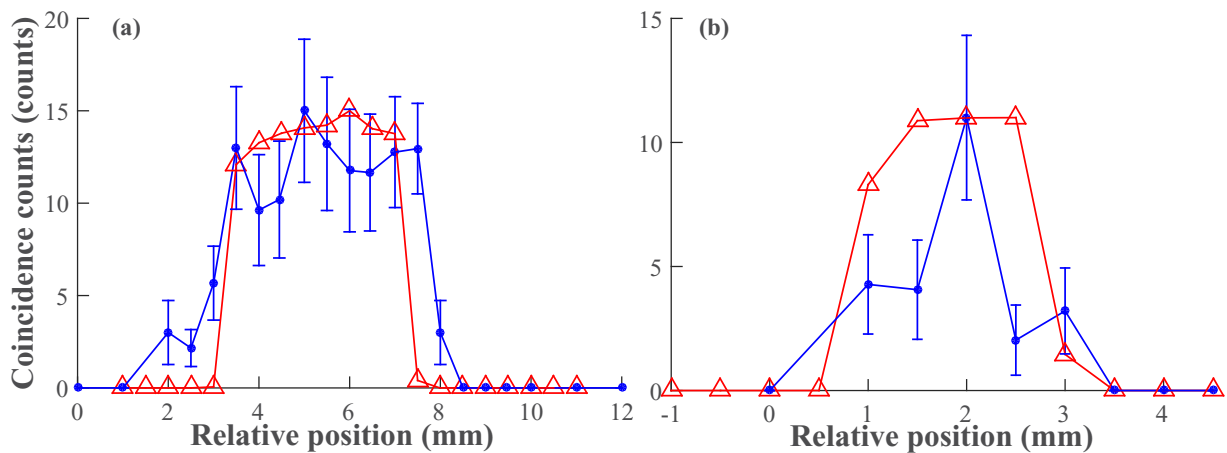


FIG. 4. Ghost imaging of (a) 4-mm and (b) 2-mm slits. The blue circles are the data that constitute the ghost imaging and the red triangles are direct imaging measurements by using a scanning slit behind the object. The coincidence counts in the ghost imaging plots are scaled to the geometry of the detector (see text for more details). The direct imaging measurements are taken with $\sim 10^6$ counts per slit position and scaled to the peaks of the ghost images. The solid lines are guides for the eye. The error bars are estimated by assuming a Poisson distribution.

agreement within the width of the pump beam (4.75 ± 0.5 and 4 ± 0.25 mm for the GI and direct imaging of the 4 ± 0.5 -mm slit, respectively, and 2 mm and 2 ± 0.25 mm for the GI and direct imaging of the 2-mm slit, respectively). Due to the narrow energy bandwidth the average coincidence count rate in our measurements is only about seven photon pairs per hour. It is clear from the results that the background level is nominally zero. It is also clear from the results that our scheme is well suited to measurements with extremely low count rates, which can be advantageous for a variety of quantum optics experiments. This is due to the extremely low noise of x-ray detectors and the use of coincidences and the energy resolution of our detection system. We note that even with the low statistics of up to ten photons per slit position in the GI results in panel (b) of Fig. 4, the width of the slit is already discernible.

III. CONCLUSION

In summary, we reported the observation of GI by utilizing x-ray photon pairs. Here we have demonstrated an application of x-ray pairs that are generated by the process of PDC.

The strong and clear anticorrelations between the k -vectors we have shown suggest that it would be possible to use our procedure to observe quantum optics effects at x-ray wavelengths. For example, by using a smaller scanning slit or a two-dimensional (2D) detector [32] with a small pixel size, it would be possible to measure the near-field correlations and the far-field correlations simultaneously [26]. Further suppression of the fluorescence background will allow the measurement of the signal and idler photons without coincidences, which will likely lead to sub-shot-noise measurements [12]. The quality of the ghost imaging can be further improved by using new emerging high-repetition-rate free-electron lasers such as the European XFEL [33] and LCLS-II-HE [34]. Finally, in this work we demonstrated the ability to measure x-ray photon pairs with a negligible background level, which opens the possibilities to observe quantum optics with x-ray photon pairs. As a consequence, we expect that the extension of our procedure can be used for the observation of single heralded photons, which can be used for experiments in quantum x-ray optics [35,36]. Another promising extension of the scheme we present is the demonstration of two-photon x-ray diffraction [37].

ACKNOWLEDGMENTS

We acknowledge the SPring8 Facility for provision of synchrotron radiation facilities. This work was supported by the Israel Science Foundation (ISF)(IL), Grant No. 201/17.

This research was supported by a Marie Curie FP7 Integration Grant within the 7th European Union Framework Programme under Grant Agreement No. PCIG13-GA-2013-618118. D.B. gratefully acknowledges support by the Ministry of Aliyah and Immigrant Absorption of Israel.

APPENDIX

1. Experimental details

We provide further details on the experimental setup and on the procedures that we describe in the main text.

First, we elaborate on the experimental setup. The average input power is $\sim 5 \times 10^{13}$ photons/s and its polarization is in the scattering plane. The input beam is monochromatic at 22.3 keV. The nonlinear crystal is a 4 mm \times 4 mm \times 0.8 mm diamond crystal. The Bragg angle is 41.5° . The pump deviation from the Bragg angle at the phase-matching condition is 10 mdeg. The degenerate photon energies of the signal and idler are 11.15 keV, where the angular separation between the detectors is $\sim 2.1^\circ$. We use helium ducts, which are mounted between the nonlinear crystal and the detectors to reduce the air absorption of the PDC photon pairs.

Next, we describe the coincidence electronics as shown in Fig. 5. Each of the detectors provides a logical output signal that is used as an input to an AND gate. The output of the AND gate is used to trigger the digitizer and determines the width of the time window of each coincidence event. The width of the time window in our setup is 120 ns. For each event that is within the time window, the analog signals of the two detectors, which are proportional to the detected photon energies, are recorded with a digitizer (PicoScope 6000). The values of the photon energies of the two detectors are calibrated according to the incident pump energy. The raw data of the digitizer trace of the analog signals are corrected by using dc subtraction according to the voltage levels at the tail of the pulses of the analog signals.

2. Resolving the slit size from the spectra

We show that it is possible to use the measured coincidence spectra to resolve the widths of slits without using any direct spatial measurement. For this purpose, we utilize the one-to-one correspondence between the photon energies and the k -vector directions of the photon pairs as is illustrated in Fig. 1(b). Panels (a) and (b) of Fig. 6 show the total coincidence spectra of 4- and 2-mm slits, respectively. The blue bars are the experimental results and the solid red lines are calculated from theory and scaled to the peak of the spectra. Since we sum over the different positions of the reference slit, each

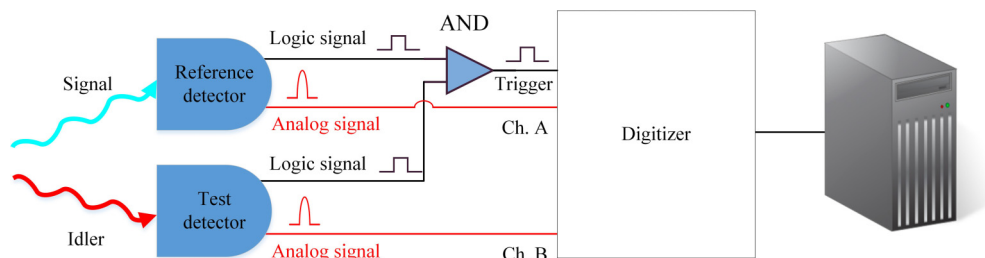


FIG. 5. Schematic of the electronic setup.

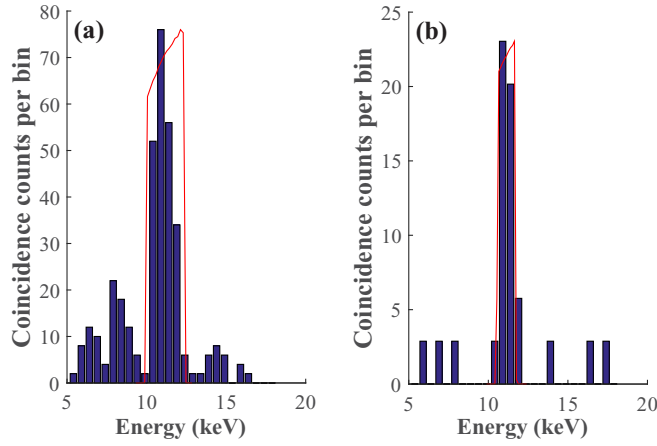


FIG. 6. Slits size from spectra: Reference detector photon energy spectra of the coincidence counts of (a) 4-mm slit and (b) 2-mm slit. The histograms are constructed by summing up the data at the different positions of the reference slit. The blue bars are the experimental results and the solid red lines are calculated from theory and scaled to the peak of each of the spectra. The accidental coincidences on the right and left of the coincidence spectra are a consequence of summing over the entire spectra and the different positions of the reference slit.

spectrum in Fig. 6 is equivalent to a measurement with a large area reference detector. Hence, the bandwidth of each spectrum is determined by the size of the test slit due to the one-to-one correspondence between the photon energies and the k -vector directions of the photon pairs. The experimental results in panels (a) and (b) of Fig. 6 are in agreement with the numerical simulations. The PDC spectra can therefore be used to measure the support of objects even without using the spatial resolution of the reference detector. The spectra in Fig. 6 are generated by summing up over the counts of the energy histograms at the reference detector positions of 3–6.5 mm in panel (a) and 1–3 mm in panel (b).

3. Details of the theoretical calculations

We provide a further mathematical description of the wave equation model that we use for the comparison with the experimental results.

The nonlinear current density at a geometry where the angles between the signal and the idler with respect to the pump are close to 90° , which we use in our numerical simulations, can be expressed as follows [9]:

$$J_s^{\text{NL}}(\omega_s = \omega_p - \omega_i) = -\frac{e\rho_g E_p E_i^*}{4m_e^2 \omega_p^2 \omega_i} (\vec{G} \cdot \hat{e}_p)(\hat{e}_i \cdot \hat{e}_s), \quad (\text{A1})$$

where m_e and e are the electron mass and charge, respectively; \vec{G} is the reciprocal lattice vector orthogonal to the atomic planes, and E_i and E_p are the electric fields of the idler and the pump, respectively; \hat{e}_p , \hat{e}_s , and \hat{e}_i are the polarizations of the pump, the signal and the idler, respectively; ω_p , ω_s , and ω_i are the angular frequencies of the pump, the signal, and the idler, respectively; $\rho_0 = \rho_g \exp(i\vec{G} \cdot \vec{r})$ is the charge density in the absence of the pump.

Under the assumptions of undepleted pump approximation and slowly varying envelope approximation (SVEA), the coupled wave equations describing the PDC process in the

frequency domain can be described as [8,9]

$$\begin{aligned} \frac{\partial a_s}{\partial z} + \frac{\alpha_s}{\cos \theta_s} a_s &= -\kappa' a_i^+ \exp[i\Delta k_z z] + \sqrt{\frac{2\alpha_s}{\cos \theta_s}} f_s, \\ \frac{\partial a_i^+}{\partial z} + \frac{\alpha_i}{\cos \theta_i} a_i^+ &= -\kappa'^* a_s \exp[-i\Delta k_z z] + \sqrt{\frac{2\alpha_i}{\cos \theta_i}} f_i^+ \end{aligned} \quad (\text{A2})$$

where α_s and α_i are the absorption coefficients at the signal and idler wavelengths, respectively; θ_s and θ_i are the signal and idler angles with respect to the atomic planes, respectively; and Δk_z is the phase mismatch along the z axis; $f_s(z, \vec{q}, \omega)$ and $f_i^+(z, \vec{q}, \omega)$ are the Langevin noise operators; $\kappa' = \frac{i\kappa}{\sqrt{\cos \theta_s \cos \theta_i}}$, where $\kappa = \frac{(2\hbar\eta_p \eta_s \eta_i \omega_p \omega_s \omega_i)^{1/2} J_s^{\text{NL}}}{2\omega_s E_i^*}$ is the nonlinear coupling coefficient.

The time-space signal and idler operators are related to their frequency domain counterparts by

$$\begin{aligned} a_s(z, \vec{r}, t) &= \int_0^\infty \int_{-\infty}^\infty a_s(z, \vec{q}, \omega) [-i(\vec{q} \cdot \vec{r} - \omega t)] dq d\omega, \\ a_i(z, \vec{r}, t) &= \int_0^\infty \int_{-\infty}^\infty a_i(z, \vec{q}, \omega) [-i(\vec{q} \cdot \vec{r} - \omega t)] dq d\omega, \end{aligned} \quad (\text{A3})$$

where $\vec{r} = (x, y)$. The commutation relations for the signal and idler operators are

$$\begin{aligned} [a_j(z_1, \vec{q}_1, \omega_1), a_k^+(z_2, \vec{q}_2, \omega_2)] \\ = \frac{1}{(2\pi)^3} \delta(z_1 - z_2) \delta(\vec{q}_1 - \vec{q}_2) \delta(\omega_1 - \omega_2). \end{aligned} \quad (\text{A4})$$

Here $\vec{q}_j = (k_{jx}, k_{jy})$, where k_{jx} and k_{jy} represent the k wave-vector components parallel to the surfaces of the crystal. The signal count rate is given by $\langle a_s^\dagger(z, \vec{r}_2, t_2) a_s(z, \vec{r}_1, t_1) \rangle$.

The coincidence count rate for ghost imaging can be considered as follows:

$$\begin{aligned} R_c &= A(2\pi)^6 \iiint \langle a_i^+(\omega_1, k_{x1}, k_{y1}) a_s^+(\omega_2, k_{x2}, k_{y2}) \\ &\times a_s(\omega_2, k_{x2}, k_{y2}) a_i(\omega_1, k_{x1}, k_{y1}) \rangle \\ &\times |H(\omega_1)|^2 |H(\omega_2)|^2 |H(k_{x1})|^2 |H(k_{x2})|^2 |H(k_{y1})|^2 \\ &\times |H(k_{y2})|^2 d\omega_1 d\omega_2 dk_{x1} dk_{x2} dk_{y1} dk_{y2} \end{aligned} \quad (\text{A5})$$

where A is the effective spot size of the pump; 1 and 2 are the indices of the two detectors, respectively; and H is the window function of the object.

4. Simulation details

The parameters of the simulations that lead to the theoretical results corresponding to Figs. 2 and 3 are the horizontal and vertical reference detector acceptance angles of 0.48 and 5.4 mrad, respectively.

The offset values of the detector angles from the phase-matching solutions at the degeneracy in Figs. 2 and 3 are determined according to the different positions of the reference detector with respect to the center of the GI image, which we define as the phase-matching condition at the degeneracy.

The parameters of the simulations that lead to the theoretical results corresponding to Fig. 6(a) are the horizontal and vertical test detector acceptance angles of 3.8 and 5.4 mrad,

respectively. The parameters of the simulations that lead to the theoretical results corresponding to Fig. 6(b) are the horizontal

and vertical test detector acceptance angles of 1.9 and 5.4 mrad, respectively.

-
- [1] M. O. Scully and M. S. Zubairy, *Quantum Optics* (Cambridge University Press, Cambridge, 1997).
- [2] D. F. Walls and G. J. Milburn, *Quantum Optics* (Springer, New York, 2008).
- [3] C. C. Knight and P. L. Gerry, *Introductory Quantum Optics* (Cambridge University Press, New York, 2007).
- [4] M. I. Kolobov, *Quantum Imaging* (Springer, New York, 2007).
- [5] P. M. Eisenberger and S. L. McCall, *Phys. Rev. Lett.* **26**, 684 (1971).
- [6] Y. Yoda, T. Suzuki, X. W. Zhang, K. Hirano, and S. Kikuta, *J. Synchrotron Rad.* **5**, 980 (1998).
- [7] B. W. Adams, *Nonlinear Optics, Quantum Optics, and Ultrafast Phenomena with X-Rays* (Kluwer Academic Publisher, Norwell, MA, 2008).
- [8] S. Schwartz, R. N. Coffee, J. M. Feldkamp, Y. Feng, J. B. Hastings, G. Y. Yin, and S. E. Harris, *Phys. Rev. Lett.* **109**, 013602 (2012).
- [9] D. Borodin, A. Schori, F. Zontone, and S. Schwartz, *Phys. Rev. A* **94**, 013843 (2016).
- [10] S. Schwartz and S. E. Harris, *Phys. Rev. Lett.* **106**, 080501 (2011).
- [11] G. B. Lemos, V. Borish, G. D. Cole, S. Ramelow, R. Lapkiewicz, and A. Zeilinger, *Nature* **512**, 409 (2014).
- [12] G. Brida, M. Genovese, and I. R. Berchera, *Nat. Photonics* **4**, 227 (2010).
- [13] T. B. Pittman, Y. H. Shih, D. V. Strekalov, and A. V. Sergienko, *Phys. Rev. A* **52**, R3429 (1995).
- [14] P. A. Morris, R. S. Aspden, J. E. Bell, R. W. Boyd, and M. J. Padgett, *Nat. Commun.* **6**, 5913 (2015).
- [15] R. S. Aspden, N. R. Gemmell, P. A. Morris, D. S. Tasca, L. Mertens, M. G. Tanner, R. A. Kirkwood, A. Ruggeri, A. Tosi, R. W. Boyd, G. S. Buller, R. H. Hadfield, and M. J. Padgett, *Optica* **2**, 1049 (2015).
- [16] F. Kaneda, B. G. Christensen, J. J. Wong, H. S. Park, K. T. McCusker, and P. G. Kwiat, *Optica* **2**, 1010 (2015).
- [17] M. N. O'Sullivan, Kam Wai Clifford Chan, and R. W. Boyd, *Phys. Rev. A* **82**, 053803 (2010).
- [18] F. Ferri, D. Magatti, V. G. Sala, and A. Gatti, *Appl. Phys. Lett.* **92**, 261109 (2008).
- [19] F. Ferri, D. Magatti, A. Gatti, M. Bache, E. Brambilla, and L. A. Lugiato, *Phys. Rev. Lett.* **94**, 183602 (2005).
- [20] R. S. Bennink, S. J. Bentley, and R. W. Boyd, *Phys. Rev. Lett.* **89**, 113601 (2002).
- [21] D. Pelliccia, A. Rack, M. Scheel, V. Cantelli, and D. M. Paganin, *Phys. Rev. Lett.* **117**, 113902 (2016).
- [22] H. Yu, R. Lu, S. Han, H. Xie, G. Du, T. Xiao, and D. Zhu, *Phys. Rev. Lett.* **117**, 113901 (2016).
- [23] A. Schori and S. Schwartz, *Opt. Express* **25**, 14822 (2017).
- [24] D. Pelliccia, M. P. Olbinado, A. Rack, and D. M. Paganin, [arXiv:1710.00727](https://arxiv.org/abs/1710.00727).
- [25] A.-X Zhang, Y.-H. He, L.-A. Wu, L.-M. Chen, and B.-B. Wang, *Optica* **5**, 374 (2018).
- [26] J. C. Howell, R. S. Bennink, S. J. Bentley, and R. W. Boyd, *Phys. Rev. Lett.* **92**, 210403 (2004).
- [27] R. Röhlberger, H. C. Wille, K. Schlage, and B. Sahoo, *Nature* **482**, 199 (2012).
- [28] R. Röhlberger, K. Schlage, B. Sahoo, S. Couet, and R. Ruffer, *Science* **328**, 1248 (2010).
- [29] F. Vagizov, V. Antonov, Y. V. Radeonychev, R. N. Shakhmuratov, and O. Kocharovskaya, *Nature* **508**, 80 (2014).
- [30] J. Haber, X. Kong, C. Strohm, S. Willing, J. Gollwitzer, L. Bocklage, R. Ruffer, A. Pálffy, and R. Röhlberger, *Nat. Photonics* **11**, 720 (2017).
- [31] M. Yabashi, T. Mochizuki, H. Yamazaki, S. Goto, H. Ohashi, K. Takeshita, T. Ohata, T. Matsushita, K. Tamasaku, Y. Tanaka, and T. Ishikawa, *Nucl. Instrum. Methods Phys. Res., Sect. A* **467**, 678 (2001).
- [32] B. M. Jost, A. V. Sergienko, A. F. Abouraddy, B. E. Saleh, and M. C. Teich, *Opt. Express* **3**, 81 (1998).
- [33] S. Serkez, G. Geloni, S. Tomin, G. Feng, E. V. Gryzlova, A. N. Grum-Grzhimailo, and M. Meyer, *J. Opt.* **20**, 024005 (2018).
- [34] R. W. Schoenlei, S. Boutet, M. P. Minitti, and A. M. Dunne, *Appl. Sci.* **7**, 850 (2017).
- [35] S. A. Castelletto and R. E. Scholten, *Eur. Phys. J. Appl. Phys.* **41**, 181 (2008).
- [36] M. D. Eisaman, J. Fan, A. Migdall, and S. V. Polyakov, *Rev. Sci. Instrum.* **82**, 071101 (2011).
- [37] J. Stöhr, *Phys. Rev. Lett.* **118**, 024801 (2017).